arXiv:1704.01543v1 [physics.space-ph] 5 Apr 2017

Turbulence Associated with Magnetopause Reconnection

L. Price and M. Swisdak
IREAP, University of Maryland, College Park MD 20742-3511, USA

J. F. Drake
Department of Physics, the Institute for Physical Science and Technology and the Joint Space Science Institute, University of Maryland, College Park MD 20742-3511, USA

J. L. Burch
Southwest Research Institute, San Antonio, Texas, 78228, USA

P. A. Cassak
Department of Physics and Astronomy, West Virginia University, Morgantown, West Virginia 26506, USA

R. E. Ergun
Department of Astrophysical and Planetary Sciences, University of Colorado, Boulder, Colorado, 80303, USA

We present detailed analysis of the turbulence observed in three-dimensional particle-in-cell simulations of magnetic reconnection at the magnetopause. The parameters are representative of an electron diffusion region encounter made by the Magnetospheric Multiscale (MMS) mission. The turbulence is found to develop around both the magnetic x-line and separatrices, is electromagnetic in nature, is characterized by a wavevector k given by $k\rho_e \sim (m_e/m_i)^{0.25}$ with ρ_e the electron Larmor radius, and appears to have the ion pressure gradient as its source of free energy. Taken together, these results suggest the instability is a variant of the lower-hybrid drift instability. The turbulence produces electric field fluctuations in the out-of-plane direction (the direction of the reconnection electric field) with an amplitude of around ± 10 mV/m, which is much greater than the reconnection electric field of around 0.1 mV/m. Such large values of the out-of-plane electric field have been identified in the MMS data. The turbulence in the simulations controls the scale lengths of the density profile and current layers in asymmetric reconnection, driving them closer to $\sqrt{\rho_e \rho_i}$ than the ρ_e or d_e scalings seen in 2D reconnection simulations.

I. INTRODUCTION

During magnetic reconnection topological changes in the magnetic field trigger the transfer of magnetic energy to the surrounding plasma, where it appears as flows, thermal energy, and non-thermal particles. The change of topology occurs at magnetic x-lines, which are embedded within electron diffusion regions. The recently launched Magnetospheric Multiscale (MMS) mission is designed to make high-resolution spatial and temporal measurements within electron diffusion regions and explore the small-scale activity, including turbulence, found there [2].

The initial phase of the MMS mission focused on the magnetopause, the location where the plasmas of the magnetosheath and magnetosphere reconnect. Such reconnection is typically asymmetric [3] and includes significant differences between the magnetic fields, densities, and ion and electron temperatures. The large gradients associated with these asymmetries are susceptible to the generation of drift waves and their associated instabilities. Of particular interest for reconnection, which produces ambient gradients with scale lengths at or below the ion Larmor radius ρ_i or ion inertial scale d_i, is the lower-hybrid drift instability (LHDI). The theory of this instability has been widely explored in previous work [4, 5, 8, 15, 16, 18].

The fundamental energy sources for LHDI are magnetic field and plasma pressure inhomogeneities that drive the relative drifts of electrons and ions. In the case of the magnetopause the relative drift of the electrons and protons arises dominantly from the $\mathbf{E} \times \mathbf{B}$ drift of electrons: the ion pressure across the magnetopause is to lowest order balanced by a Hall electric field

$$E_x \sim \frac{1}{ne}\frac{\partial P_i}{\partial x} \sim \frac{P_i}{neL_i} \tag{1}$$

with P_i the ion pressure and L_i the ion pressure scale length (we use GSM coordinates with x pointing toward the sun, y pointing in the azimuthal direction and z pointing to the North). The consequence is that to lowest order the ion drift in the y direction is zero (there is no ion diamagnetic drift) and the Hall electric field drives a current of electrons

$$v_{de} \sim \frac{cE_x}{B_z} \sim \frac{cT_i}{eB_z L_i} \sim v_{*i} \tag{2}$$

in the y direction that is equal in magnitude to the ion diamagnetic velocity $v_{*i} = v_i \rho_i / L_i$. This strong drift is reflected in the crescent-shaped electron velocity distributions documented in MMS observtions [2]. Because $T_i \gg T_e$ at the magnetopause electron diamagnetic drifts

are small compared with this $\mathbf{E}\times\mathbf{B}$ drift. Thus, it is fundamentally the ion pressure gradient that is the driver of the relative drift of ions and electrons and the driver of drift-type instabilities. On the other hand, the ion-pressure-driven electron drift and associated current supports the reversal in the direction of the magnetic field across the magnetopause. Because the system is inductive, the integral of the current across the reversal is an invariant and the magnetic free energy becomes the effective energy source for driving drift instabilities.

In the low-β "local approximation" (for which the profiles of pressure and current are neglected) the basic characteristics of LHDI are: electrostatic oscillations, $\mathbf{k}\cdot\mathbf{B}=0$, a most unstable mode satisfying $k\rho_e\sim 1$, and $\omega\sim kv_{*i}\sim\Omega_{\rm lh}$. Here ω is the mode frequency, k is the wavenumber, ρ_e is the electron Larmor radius and $\Omega_{\rm lh}=\sqrt{\omega_{ce}\omega_{ci}}$ is the lower hybrid frequency.

However these properties are modified when the LHDI is excited in a narrow current sheet (one with a width of order the ion gyroradius or smaller). Theory and simulations [4, 16] suggest the "local" mode described above quickly saturates and another longer-wavelength instability subsequently develops. The new LHDI mode is electromagnetic and has a wavenumber $k\rho_e\sim(m_eT_e/m_iT_i)^{0.25}$. In addition, while the shorter wavelength electrostatic fluctuations tends to be confined to the edges of the current sheet (being stabilized at high $\beta=8\pi P/B^2$), the longer wavelength electromagnetic mode penetrates to the sheet's center. Moreover, the electromagnetic mode need not strictly satisfy $\mathbf{k}\cdot\mathbf{B}=0$.

In a previous paper [12] we performed a three-dimensional simulation of reconnection with initial conditions representative of an MMS observation of an electron diffusion region [2]. As part of that work we observed turbulence developing around both the x-line and the separatrices and showed that the turbulence was strong enough to contribute an effective "anomalous resistivity" and "anomalous viscosity" to Ohm's law in the electron diffusion region. We suggested that the turbulence was due to LHDI. Others have noted, however, that the turbulence measured by the MMS did not satisfy the criteria for the "local" LHDI outlined above [7]. In this work, we perform a more detailed analysis of the turbulence produced in reconnection simulations and conclude that it, in fact, shares many characteristics with the longer wavelength electromagnetic version of the LHDI. These conclusions are consistent with *Le et al.* [10], who also showed that during reconnection the instability produced significant transport across the magnetospheric separatrix.

In addition, we identify characteristics of the turbulence in our simulations that are consistent with MMS observations. Section II presents the details of the simulations, section III presents our analysis of the turbulence, and section IV discusses the results and our conclusions.

II. SIMULATIONS

We use the particle-in-cell code `p3d` [19] to perform the simulations. Lengths are normalized to the ion inertial length $d_i=c/\omega_{pi}$, where $\omega_{pi}=\sqrt{4\pi n_0e^2/m_i}$ is the ion plasma frequency, and times are normalized to the ion cyclotron time $\omega_{ci0}^{-1}=m_ic/eB_0$. A nominal magnetic field strength B_0 and density n_0 define the Alfvén speed $v_{A0}=\sqrt{B_0^2/4\pi m_in_0}$ which serves as the velocity normalization. Electric fields and temperatures are normalized to $v_{A0}B_0/c$ and $m_iv_{A0}^2$, respectively.

A simulation presented here was first discussed in *Price et al.* [12]. Its initial conditions mimic the observations by MMS of a magnetopause diffusion region encounter on 16 October 2015 that is described in *Burch et al.* [2]. We use the right-handed LMN coordinate system, in which L is in the direction of the reconnecting magnetic field (roughly north-south), N parallels the inflow direction (roughly radial), and M (roughly azimuthal) is perpendicular to L and N in the out-of-plane direction. The particle density n, reconnecting magnetic field component B_L, and ion temperature T_i vary as functions of N with hyperbolic tangent profiles of width 1. The asymptotic values of n, B_L, and T_i are 1.0, 1.0, and 1.37 in the magnetosheath and 0.06, 1.70, and 7.72 in the magnetosphere. The small guide field, $B_M=0.099$, is initially uniform. The profile of the electron temperature T_e is determined by pressure balance, with the asymptotic values fixed to 0.12 in the magnetosheath and 1.28 in the magnetosphere. While in pressure balance this choice of initial conditions is not a Vlasov (kinetic) equilibrium. However, any evolution due to this lack of equilibrium is quickly overwhelmed by the development of reconnection and turbulence.

We perform two three-dimensonal simulations of this system, with computational domains of dimensions $(L_L,L_M,L_N)=(40.96,10.24,20.48)$ and $(20.48,5.12,10.24)$. The simulations have the same asymptotic plasma parameters and only differ in computational parameters, namely the ion-to-electron mass ratio, the grid resolution, and the speed of light. The mass ratios are chosen to be 100 and 400, respectively, which eases the computational expense associated with using the true mass ratio yet is sufficient to separate the ion d_i and electron d_e scales ($d_e=0.1d_i$ and $0.05d_i$, respectively). Note that although the computational domains differ in size when measured in d_i, they are the same size when measured in electron scales (d_e or ρ_e).

The spatial grid has resolutions of $\Delta=0.02$ and $\Delta=0.01$, respectively, which resolve the system's smallest physical scale, the Debye length in the magnetosheath, ≈ 0.03. We use 50 particles per cell per species when $n=1.0$ and, as this implies ≈ 3 particles per cell in the low-density magnetosphere, our analysis employs, when necessary, averages over multiple cells to mitigate the resulting noise. The speed of light is chosen to be $c=15$ and 30 respectively, and our boundary conditions are periodic in all directions. A small perturbation is added

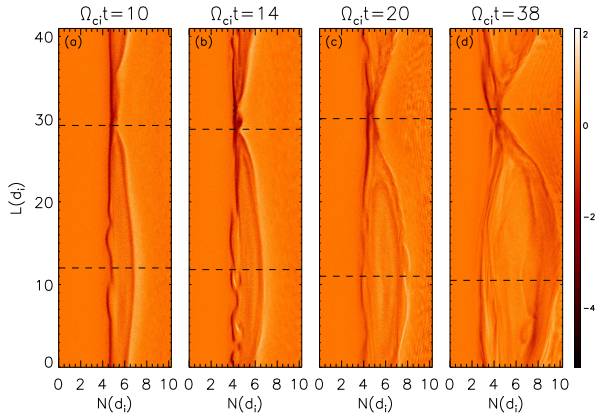

FIG. 1. Snapshots of J_{eM}, the dawn-dusk electron current density, in one $L-N$ plane. Panels (a-d) are taken at $t = 10$, 14, 20, and 38, respectively. These times highlight the onset of the instability, the time of maximum growth, the beginning of the saturated non-linear state, and the end of the simulation. The colors in each panel are identically normalized, with the color bar at the right showing the range. The dashed lines in each panel indicate the locations of cuts through the x-line and island presented in Figure 2.

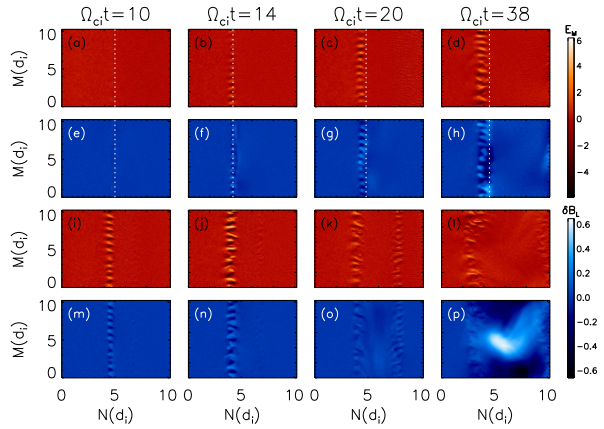

FIG. 2. Snapshots of E_M (a-d, i-l), the electric field in the direction of the reconnection-associated current, and δB_L (e-h, m-p), the fluctuations in the reconnecting magnetic field, in the $M-N$ plane at the same times as in Figure 1. The cuts were taken at the positions shown by the dashed lines in Figure 1. Panels (a-h) are taken at the L location of the x-line, while panels (i-p) are taken through the middle of the island. The red color bar corresponds to E_M, while the blue color bar corresponds to δB_L. The dotted lines in panels (a-h) correspond to the N location of the x-line.

to initialize reconnection. Companion two-dimensional simulations show that reducing the size of this perturbation by a factor of two has no significant effect other than delaying the onset of reconnection. Unless otherwise stated, the subsequent figures and discussion focus on the larger simulation with $m_i/m_e = 100$.

III. ANALYSIS

In two-dimensional simulations, where variations in the out-of-plane (M) direction are suppressed, reconnection in this system remains laminar [12]. In contrast, the additional freedom present in three-dimensional simulations allows modes to develop with finite k_M. Figure 1 displays images of J_{eM}, the dawn-dusk electron current density, in a single $L-N$ plane at four representative times. The reason for choosing these times will be discussed further below, but they roughly correspond to the onset of the instability, the time of maximum growth, the beginning of the saturated non-linear state, and the end of the simulation. The magnetosphere (strong field, low density, high temperature) is to the left and the magnetosheath (weak field, high density, low temperature) to the right. The results exhibit the typical features of asymmetric reconnection, including the bulge of the magnetic islands into the low-field-strength magnetosheath and the separation between the x-point and the stagnation point of the fluid flow [3, 12]. As can be seen in panel (a), turbulence first develops along the magnetospheric separatrix before developing at the x-line (panel (b)) and the magnetosheath separatrix (panels (c) and (d)). Images from other $L-N$ planes exhibit similar features.

The instability driving the turbulence is electromagnetic in nature, as can be seen in Figure 2. Panels (a-h) show E_M and δB_L in the $M-N$ plane that cuts through the x-line, while panels (i-p) show the same quantities along a cut through the island. Here, δB_L is the fluctuating component of B_L, i.e., $\delta B_L = B_L - \langle B_L \rangle$, where $\langle B_L \rangle$ is B_L averaged over the M direction. This is the dominant magnetic field perturbation – convection of the large gradient of B_L in the initial state due to the perturbed v_{eN} leads to large fluctuations. Fluctuations of B_M and B_N are also present but at a reduced amplitude [12].

The turbulence first appears in both E_M and δB_L at $t = 10$ along the magnetospheric separatrix in panels (i) and (m). Turbulence develops at the x-line (panels (b) and (f)) and along the magnetosheath separatrix (panels (j) and (n)) by $t = 14$, though the latter is clearer by $t = 20$ (panels (k) and (o)). It is interesting to note that, even at relatively early times, the location of the turbulence begins to shift away from the x-line, denoted by the white dotted lines in panels (a-h), towards the magnetosphere. We also observe evidence of a possible kink mode late in the simulation in panel (p). This mode produces a global perturbation to the current sheet, but at longer wavelength than the fluctuations seen in the other panels.

The wavelength of the drift instability can be directly measured in several of the panels. In Figure 2(c), for example, there are 11 wavelengths present in the M direction (length $10.24 d_i$). In our mass-ratio 100 simulation $1 d_i \approx 20 \rho_e$, which gives $k_M \rho_e \approx 0.33$. As will be discussed later, this is consistent with the expectation for long wavelength LHDI.

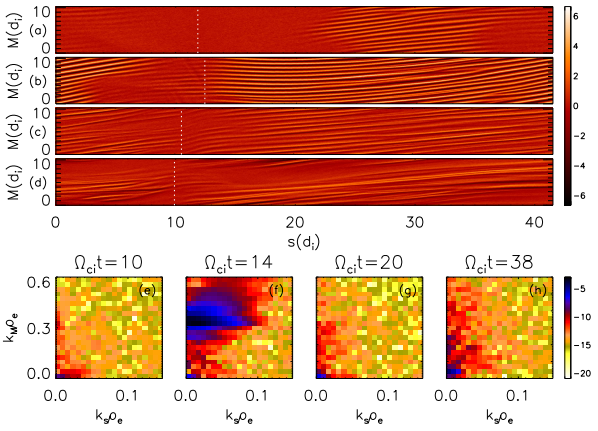

FIG. 3. $E_M(s, M)$ (panels (a)-(d)) and Fourier transforms (panels (e)-(h)) at the same times as in Figure 1, where s is the distance along the average (over M) magnetic field. The data is from a surface that lies to the left (magnetospheric side) of the magnetospheric separatrix. Panel (a) shows $E_M(s, M)$ at $t = 10$; the $k_s - k_M$ power spectrum $\log(|\tilde{E}_M(k_s, k_M)|^2)$ at the same time is shown in panel (e). Panels (f), (g), and (h) are similarly paired with panels (b), (c), and (d) and show the simulation data at $t = 14$, 20, and 38, respectively. The white dotted lines in panels (a-d) correspond to the location of the x-line. Panels (a-d) are normalized to the same value, as seen in their accompanying color bar. Panels (e-h) also have a common normalization.

While LHDI is the most likely candidate to explain the turbulence seen in our simulations, the modified-two-stream instability (MTSI) can also exist in finite β systems if the relative cross-field drifts of the electrons and ions are comparable or exceed the local Alfvén speed [17]. It has been suggested that this instability is important in laboratory reconnection experiments [9]. This instability has a growth rate that peaks with a non-zero component of the wavevector along the local magnetic field $k_\parallel$ in contrast with the LHDI, which has a peak growth rate for $k_\parallel = 0$ [4]. Thus, to distinguish between the possible drivers of the turbulence, we examine its Fourier spectrum perpendicular to and along the local magnetic field in $k_\perp - k_\parallel$ space, where $k_\perp$ is calculated from the data along the M direction. Since the local direction of the magnetic field varies in space, the necessary data must be taken while following a magnetic field line. Furthermore, since the actual field lines have chaotic trajectories [12], the analysis is carried out using the magnetic field components obtained by averaging over the M direction. The averaged magnetic field on the magnetospheric side of the reconnection layer follows the separatrix between the upstream and reconnected plasma, while M points in the perpendicular direction. Choosing s to represent the distance measured along the field, we construct $E_M(s, M)$ while traveling along a field line just outside the separatrix. The range of s is chosen in order to travel through the simulation domain in the L direction exactly once. This data is not periodic in s for a given value of M but the data can be extended arbitrary distances along s by stacking the data along s if it is shifted a fixed distance in M.

The resultant $E_M(s, M)$ at four times can be seen in Figure 3(a-d). The primarily horizontal stripes correspond to the same instability shown in Figure 2. In panel (a), calculated at $t = 10$, the instability is weak at the location of the x-line (the white dotted line), but strong near the middle of the island (see Figure 1a). By $t = 14$ in panel (b) the instability is present at all values of s, including at the x-line, although it remains strongest near the middle of the island. This pattern persists at later times, $t = 20$ and 38, panels (c) and (d) respectively, making it appear that the turbulence near the x-line is not strong. However note that, as seen in Figure 2(c) and (d), the turbulence at these times is displaced from the separatrix. Although not shown here, $E_M(s, M)$ at the x-line is much stronger along a trajectory that is displaced toward the magnetosphere compared with that shown in Figure 3.

To determine the dominant wavelengths present in $E_M(s, M)$, we construct two-dimensional spatial Fourier transforms (denoted by the operator $\mathcal{F}$) of the $s - M$ domain, $\tilde{E}_M(k_s, k_M) = \mathcal{F}[E_M(s, M)]$. We plot $\log(|\tilde{E}_M(k_s, k_M)|^2)$ for the longest wavelength modes in Figure 3(e)-(h). At $t = 10$, panel (e), which is the linear stage of the instability, the spectrum is dominated by nearly-perpendicular wavevectors (note the difference in vertical and horizontal axis scales). The peak power when the instability is strongest, $t = 14$, occurs for $k_M \rho_e \approx 0.33$, consistent with the calculation based on Figure 2. By this time the spectrum has acquired a significant parallel wavevector (k_s), although it continues to be dominated by perpendicular modes. After saturation (panels (c) and (d)), however, those parallel modes diminish in strength. With an ion-to-electron mass ratio of 100, theory suggests that the longer wavelength LHDI mode has $k_M \rho_e \sim (m_e/m_i)^{0.25} \approx 0.32$, which is in very close agreement with our measured value of $k_M \rho_e \approx 0.33$. (This comparison neglects the fact that $T_i \neq T_e$ which will have a modest effect on the theoretical value.)

The non-local structure of the MTSI has not been explored in the literature. Nevertheless, in local models the instability peaks at $k_\parallel/k_\perp \sim \sqrt{m_e/m_i}$ [17]. For the simulation data shown in Fig. 3 in which $m_i/m_e = 100$ the spectrum should exhibit a distinct peak centered on $k_s \sim 0.1 k_M$ if it were driven by the MTSI. There is no evidence for a peak at finite $k_\parallel$ in the data of Fig. 3.

However, the data of Fig. 3 does reveal that k_s is finite. We suggest that this is a consequence of the inhomogeneity of the out-of-plane current with distance along the separatrices. As discussed in *Price et al.* [12], this instability dominantly drives flows in the $M - N$ plane. The resulting twisting of flux ropes by the vortical $M - N$ flows is similar to that inferred from MMS observations by *Ergun et al.* [6]. The strength of the vortices varies with distance along the field line (s direction) because the amplitude of the out-of-plane current J_{eM} depends on the distance from the x-line. As a consequence, the

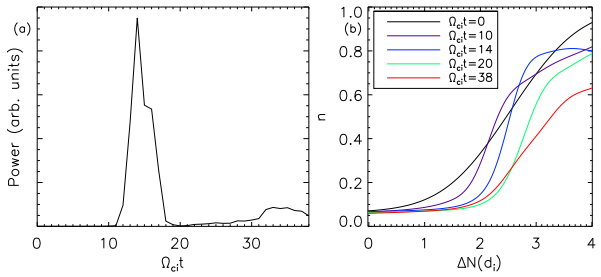

FIG. 4. Panel (a): Power in the instability based on the Fourier transforms shown in Figure 3. Panel (b): Density profiles at the x-line over time. Since the location of the density gradient changes as the islands expand, the density profiles at later times are shifted in N to ease comparisons.

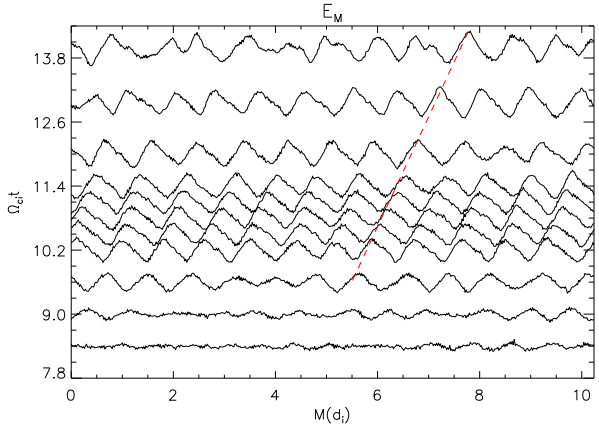

FIG. 5. Cuts of E_M along the M direction through the center of the turbulence at the magnetospheric separatrix. The vertical position of each cut is shifted based on the time at which it was taken. The red dashed line traces the displacement of one wave peak.

rate of twist of the flux tubes varies with distance from the x-line, generating non-zero values of B_M and B_N and a finite k_s.

The total power in the instability's fluctuating electric field

$$P = \sum_{k_s,k_M} |\tilde{E}_M(k_s,k_M)|^2 \qquad (3)$$

is computed for the duration of the simulation and plotted in Figure 4(a). The instability first becomes noticeable around $t = 10$, climbs rapidly to a peak at $t = 14$ and then rapidly decreases in intensity as it non-linearly saturates due to the relaxation of the driving gradients. A secondary instability, perhaps the kink mode that can be seen in the final panels of Figure 2, begins to grow, albeit more weakly, near the end of the simulation. This general pattern is not specific to the choice of E_M and is found in similar calculations performed on any component of the fluctuating electric and magnetic fields.

As discussed earlier, the energy source for the instability is the relative electron-ion drift, which is dominately produced by the ion pressure gradient. Because of the large drop in the density across the magnetopause for the initial conditions of the present simulation, the ion pressure drop is dominated by the change in density. We therefore explore the linkage between the time evolution of the density profile and the development of the turbulence to demonstrate the causal relation between the local gradient and the turbulence. Figure 4(b) shows the density profiles at the x-line for several times. Because the N location of the current sheet changes as reconnection occurs, the density profiles have been shifted to make comparisons easier. The initial density scale length L_n ($\approx 1d_i = 10d_e$ for mass-ratio 100) steepens as reconnection develops, reaching its minimum value ($L_n \approx 0.25d_i = 2.5d_e$) at $t = 14$ when the instability is strongest. The density profile then relaxes and by the end of the simulation $L_n \approx 0.5d_i = 5d_e$. This result should be contrasted with the results of 2D simulations with the same parameters (not shown), in which turbulence does not develop and in which the density gradient steepens in time and comes to a constant density scale length of around $1.0d_e$. Thus, the turbulence clearly limits the minimum density scale length and the corresponding width of the electron current layer.

Next we calculate the phase speed and frequency of the instability. Figure 5 shows cuts of E_M along the M direction through the center of the turbulence at the magnetospheric separatrix near the middle of the island. The vertical position of each cut corresponds to the time at which it was taken. The turbulence begins to appear over the background variations at $t \approx 9$ and by $t = 10$ has clearly developed linear oscillations. The topmost trace, at $t \approx 14$, is taken when the instability is strongest. The irregular variations show that it has already reached a non-linear stage. By tracing the displacement of one wave peak (the red dashed line), we determine the phase velocity of this wave to be $v_p \approx \frac{1}{2}v_A$ in the direction of the electron diamagnetic drift. This value is not specific to the wave peak chosen; similar results are obtained by translating the red dashed line in the M direction to adjacent peaks. Thus we can compute the instability frequency in the frame of the simulation $\omega = v_p k_M \approx \frac{1}{3}\Omega_{\rm lh}$.

This differs signficantly from $\Omega_{\rm lh}$, which is the textbook frequency of the LHDI. There are two reasons for this. The first is that, as discussed in *Daughton* [4], electromagnetic LHDI modes are not fixed at $\Omega_{\rm lh}$, but can instead have frequencies anywhere in the range $\omega_{\rm ci} \le \omega \le \Omega_{\rm lh}$. Second, the standard derivation of the frequency of LHDI frequency is performed in a frame with $E_N = 0$, which is not the case at the magnetopause and is not true for our simulation. In the $E_N = 0$ frame, the ions have the strongest drift, of the order of the ion diamagnetic drift velocity (which exceeds the electron diamagnetic velocity because the ions are hotter than the electrons). In our system, the ions are close to stationary, so the observed frequency is naturally lower than the lower-hybrid frequency found in the typical analysis. Fur-

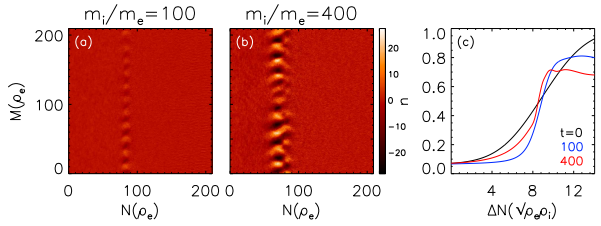

FIG. 6. Comparison between the $m_i/m_e = 100$ and 400 simulations. Panels (a-b): Snapshots of E_M in the $M - N$ plane through the x-line at times of maximum power for $m_i/m_e = 100$ (panel (a)) and 400 (panel (b)). The numerical values of E_M have been converted to units of mV/m. Panel (c): Density profiles at the x-line at $t = 0$ and times of minimum density scale length. As in Figure 4(b), the profiles have been shifted in N to facilitate comparison.

ther, the mode propagates in the electron direction. In our simulation it is not possbile to completely transform away E_N since this would require cE_N/B_L to be a constant. It is possible, however, to transform our simulation results into a frame in which the value of E_N is greatly reduced. At the magnetospheric separatrix during the time of linear evolution, $c(\mathbf{E} \times \mathbf{B})_M/B^2 \approx cE_N/B_L$ has a peak value of around $-1.7v_A$. In a frame with this velocity, the phase speed of the wave is $\approx 1.2v_A$, giving a frequency of $\omega = 0.8\Omega_{\rm lh}$, similar to the expected value. Finally, we note that waves below the lower-hybrid frequency at the magnetopause have been interpretted as arising from the LHDI [1].

In *Price et al.* [12], we suggested that the qualitative features of a real mass-ratio simulation would not differ significantly from one with $m_i/m_e = 100$. Although we find that conclusion still holds, there are important quantitative differences between the simulation discussed in detail above (mass ratio of 100) and one with mass ratio 400. Figure 6(a-b) shows E_M in the $M - N$ plane through the x-line for mass ratio 100 (panel (a)) and 400 (panel (b)) at times of maximum power (as determined using equation 3). While the simulation domains differ in size when measured in d_i, they are equivalent when measured in ρ_e. The instability is stronger in the mass ratio 400 case and the turbulence has a greater spread in the N direction. As before, the wavelength of the instability can be visually determined. In Figure 6(b), there are 10 wavelengths in the M direction (length $\approx 209\rho_e$), giving $k_M\rho_e \approx 0.30$. In agreement with theoretical expectations there are fewer wavelengths (10 versus 11) and smaller $k_M\rho_e$ for the more realistic mass ratio. Furthermore, by constructing $E_M(s, M)$ and $\log(|\tilde{E}_M(k_s, k_M)|^2)$ (not shown), we find that the peak of the instability occurs at $k_M\rho_e \approx 0.29$. For an ion-to-electron mass ratio of 400, the longer wavelength LHDI mode is expected to satisfy $k_M\rho_e \sim (m_e/m_i)^{0.25} \approx 0.22$. Note though that, as discussed below, the ambient density gradient also varies between the two simulations so the scaling $k_M\rho_e \sim (m_e/m_i)^{0.25}$ is only approximate.

The scale lengths of the density and current layers at the magnetopause are topics of scientific interest since they are linked to the processes that limit the electron current. As noted previously, our 2D simulations show that density scale length is of order $1d_e$, which is the expected value in non-turbulent reconnection. The current layers in the 3D simulations are limited by the development of turbulence and never reach electrons scales. Because our simulations are carried out with artificial mass ratios, care must be taken in interpreting the data. In Figure 6(c) we display density profiles at the x-line, similar to Figure 4(b), for our mass-ratio 100 and 400 simulations. The initial density profile is the same for both simulations. The profiles displayed for each mass ratio are chosen to correspond to the time when the density gradient is greatest. The horizontal length scale is measured in hybrid units, $\sqrt{\rho_i\rho_e}$. Thus, the minimum scale length of the density profile (and the current profile) during reconnection at the magnetopause appears to scale as the hybrid of the electron and ion Larmor radii rather than either the electron or ion scale. However, because of the weak dependence of this scaling on the mass ratio and the limited mass ratios explored in the simulations, there is some uncertainty in this conclusion. Nevertheless, the current and density scale lengths at the magnetopause are significantly greater than the expected d_e or ρ_e scale. Further, the widths are comparable to measurement of the widths of current layers during symmetric reconnection in the magnetosheath [11] and in a laboratory reconnection experiment [14].

IV. DISCUSSION

Previous analysis of three-dimensional simulations of the 16 October 2015 MMS event [12] considered the effects of the turbulence on reconnection by evaluating the contributions of various terms to an averaged Ohm's law measured within the electron diffusion region. This average was performed over the entire M dimension and eliminated the first-order turbulent contributions in order to isolate the terms relevant to large-scale reconnection. Averaging over the turbulent scales, however, is appropriate only when there is a sufficient spatial and temporal separations between large-scale reconnection and the ambient turbulence. This assumption is normally satisfied since the turbulence is at the ρ_e scale with a frequency $\Omega_{\rm lh}$ while large-scale reconnection takes place on time scales longer than the Alfvén transition time across the computational domain. The conclusion from the averaged Ohm's law was that turbulent effects play an essential role in balancing the reconnection electric field [12].

Before making further comparisons between the simulations and the MMS data, we must establish the correspondence between the units used in the simulation and those used in spacecraft measurements. For the asymptotic parameters of the October 16, 2015 event ($B_{L,sh} \sim 23$ nT, $B_{L,ms} \sim 39$ nT, $n_{sh} \sim 11.3/\text{cm}^3$, $n_{ms} \sim 0.7/\text{cm}^3$) with "sh" and "ms" subscripts denot-

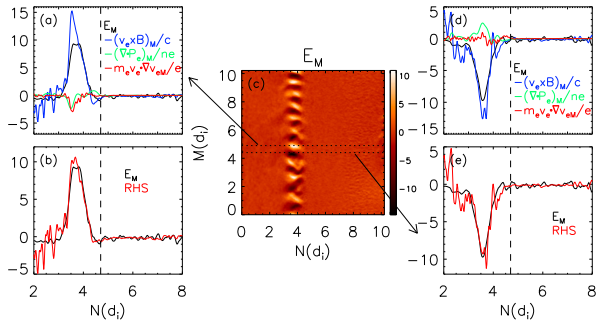

FIG. 7. Evaluation of Ohm's law on cuts through the region of instability. For direct comparison to data, values are converted from our normalized units to mV/m. Panel (a): The terms in Ohm's Law from equation 4 for a cut through $M = 4.9$. Panel (b): The sum of the left and right sides of equation 4 for $M = 4.9$. Panel (c): E_M in the $M - N$ plane at $t = 38$. The horizontal dotted lines denote locations of two cuts, at $M = 4.4$ and 4.9. Panel (d): The terms in Ohm's Law from equation 4 for a cut through $M = 4.4$. Panel (e): The sum of the left and right sides of equation 4 for $M = 4.4$. The vertical dashed lines in panels (a), (b), (d), and (e) indicate the position of the x-line.

ing the magnetosheath and magnetosphere respectively, $d_{e,sh} \sim 1.6$ km, $d_{i,sh} \sim 68$ km, $\omega_{ce,sh} \sim 4.05$ kHz, $\Omega_{\mathrm{lh},sh} \sim 95$ Hz, $\omega_{ci,sh} \sim 2.2$ Hz, $v_{A,sh} \sim 150$ km/s and $E_{0,sh} \sim 3.4$ mV/m. In our simulations we find a reconnection electric field of ~ 0.2 mV/m for either mass ratio, a value that would be very difficult to detect observationally. In fact, MMS observations reveal spikes in E_M with much larger values, peaking around ± 10 mV/m. In addition, large amplitude, short-timescale fluctuations of the parallel electric field $E_\parallel$, up to 100 mV/m, have been reported [6, 7]. These intense parallel electric fields are not observed in our simulations.

The question, then, is whether the MMS electric field measurements correspond to an effective average over the turbulence in the simulation or a slice at a particular value of M. To answer this question, note that the particle instruments on MMS directly measure the full distribution function of electrons in 30 ms and of ions in 150 ms. The frequency ω of the fluctuations in the simulation is around $\frac{1}{3}\Omega_{\mathrm{lh},sh} = 30$ Hz so the period of the waves is around 200 ms. Thus, the electron data is collected over a very short period compared to the wave period. The MMS instruments are therefore measuring the local electron Ohm's law and not the average Ohm's law that controls the global reconnection rate.

In order to model what MMS would observe on a cut through the simulation we examine the various terms in the M component of Ohm's law (the electron equation of motion)

$$E_M = -\frac{1}{c}(\mathbf{v_e}\times\mathbf{B})_M - \frac{1}{ne}(\boldsymbol{\nabla}\cdot\mathbb{P}_e)_M - \frac{1}{e}m_e\mathbf{v_e}\cdot\boldsymbol{\nabla}v_{eM} \quad (4)$$

Here $m, n, \mathbf{v_e}$ and $\mathbb{P}_e$ are the electron mass, density, velocity, and pressure tensor. In Figure 7 we present data

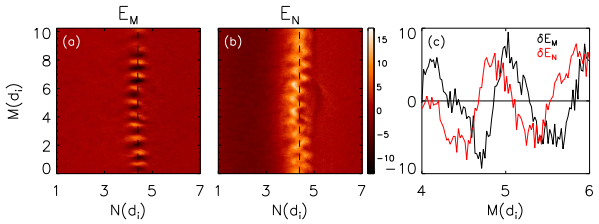

FIG. 8. E_M and E_N (panels (a) and (b), respectively) in the $M - N$ plane at the x-line at $t = 20$. For direct comparison to data, values are converted from our normalized units to mV/m. Panel (c): δE_M and δE_N through the vertical dashed line in panels (a) and (b). Panels (a) and (b) are normalized to the same value.

from two sample cuts through the electron diffusion region along the N direction that illustrate measurements characteristic of the MMS data. Figure 7(c) shows E_M near the x-line in the $M - N$ plane at $t = 38$. Panel (a) displays the separate terms in Ohm's law (Eq. 4) at $M = 4.9$ along a cut in the N direction (the upper dashed line in panel (c)). Panel (b) shows E_M and the sum of the terms from the right-hand side of equation 4. The two curves are in close agreement, which confirms that the simulation data is consistent with momentum conservation based on the electron equation of motion. Note also that the vertical scale is expressed in mV/m so the curves reflect the size of the terms that should be visible in the MMS data. Panels (d) and (e) show the same information for a cut through $M = 4.4$. The value of E_M peaks around ± 10 mV/m, very close to the values reported in the MMS data [2]. The peak value of E_M changes sign between the two cuts, which are separated by a distance roughly comparable to the distance between the MMS spacecraft. Interestingly, a similar difference in polarity is seen in the MMS data (see Figure 5 of *Burch et al.* [2]). It should be emphasized that the large value of E_M shown in these cuts is a result of the turbulence and does not reflect the rate of magnetic reconnection. The reconnection electric field, while present, is two orders of magnitude smaller and can only be extracted by the type of averaging performed in *Price et al.* [12].

As a further demonstration that E_M is primarily associated with the turbuence, Figure 8 shows E_M and E_N (panels (a) and (b)) in the $M - N$ plane near the x-line at $t = 20$. In panel (c) we plot cuts of δE_M and δE_N at the locations denoted by the vertical dashed lines in panels (a) and (b). As the current layer breaks up, it naturally produces large values of E_M and the large electron currents in the M direction are diverted into the N direction. These N-directed flows are driven by E_M. The fact that δE_M and δE_N are similar in magnitude and roughly 90° out of phase indicates that the fluctuations are linked and not due to a steady-state reconnection process. Of course, the turbulence itself might undergo reconnection on faster time scales and produce electric fields larger than the nominal value of 0.1mV/m. Such a possibility requires further analysis and comparison with

observations.

Multiple MMS observations of magnetopause electron diffusion regions have found features similar to those in Figure 7 [7]. Since the observed turbulence did not satisfy the properties of homogeneous LHDI it was suggested that some other mechanism was responsible. However, the findings presented here suggest that the governing instability has all of the characteristics of a longer wavelength version of LHDI. The instability has a dominant wavelength satisfying $k\rho_e \approx (m_e/m_i)^{0.25}$, is observed in both electric and magnetic field components and has a wavevector that is dominantly, but not strictly, perpendicular to the local magnetic field. The frequency of the instability falls in the range of frequencies unstable to LHDI, $\omega_{\rm ci} < \omega \leq \Omega_{\rm lh}$ and the growth of the instability is closely correlated with the steepening and relaxing of a density gradient (and therefore the ion pressure gradient, which is the basic driver of drift instabilities at the magnetopause). Similar instabilities have been seen in other three-dimensional reconnection simulations (albeit with different inital conditions) and were also attributed to LHDI [4, 13].

ACKNOWLEDGMENTS

This work was supported by NASA grant NNX14AC78G. We have benefited greatly from conversations with members of the MMS team. The simulations were carried out at the National Energy Research Scientific Computing Center. The data used to perform the analysis and construct the figures for this paper are available upon request.

[1] Bale, S. D., F. S. Mozer, and T. Phan (2002), Observation of lower hybrid drift instability in the diffusion region at a reconnecting magnetopause, *Geophysical Research Letters*, *29*(24), 33–1–33–4, doi:10.1029/2002GL016113, 2180.

[2] Burch, J. L., R. B. Torbert, T. D. Phan, L.-J. Chen, T. E. Moore, R. E. Ergun, J. P. Eastwood, D. J. Gershman, P. A. Cassak, M. R. Argal, S. Wang, M. Hesse, C. J. Pollock, B. L. Giles, R. Nakamura, B. H. Mauk, S. A. Fuselier, C. T. Russell, R. J. Strangeway, J. F. Drake, M. A. Shay, Y. V. Khotyaintsev, P.-A. Lindqvist, G. Marklund, F. D. Wilder, D. T. Young, K. Torkar, J. Goldstein, J. C. Dorelli, L. A. Avanov, M. Oka, D. N. Baker, A. N. Jaynes, K. A. Goodrich, I. J. Cohen, D. L. Turner, J. F. Fennell, J. B. Blake, J. Clemmons, M. Goldman, D. Newman, S. M. Petrinec, K. Trattner, B. Lavraud, P. H. Reiff, W. Baumjohann, W. Magnes, M. Steller, W. Lewis, Y. Saito, V. Coffey, and M. Chandler (2016), Electron-scale measurements of magnetic reconnection in space, *Science*, doi:10.1126/science.aaf2939.

[3] Cassak, P. A., and M. A. Shay (2007), Scaling of asymmetric magnetic reconnection: General theory and collisional simulations, *Phys. Plasmas*, *14*, 102114, doi:10.1063/1.2795630.

[4] Daughton, W. (2003), Electromagnetic properties of the lower-hybrid drift instability in a thin current sheet, *Phys. Plasmas*, *10*(3103), doi:10.1063/1.1594724.

[5] Davidson, R. C., and N. T. Gladd (1975), Anomalous transport properties associated with the lower-hybrid-drift instability, *The Physics of Fluids*, *18*(10), 1327–1335, doi:10.1063/1.861021.

[6] Ergun, R. E., K. A. Goodrich, F. D. Wilder, J. C. Holmes, J. E. Stawarz, S. Eriksson, A. P. Sturner, D. M. Malaspina, M. E. Usanova, R. B. Torbert, P.-A. Lindqvist, Y. Khotyaintsev, J. L. Burch, R. J. Strangeway, C. T. Russell, C. J. Pollock, B. L. Giles, M. Hesse, L. J. Chen, G. Lapenta, M. V. Goldman, D. L. Newman, S. J. Schwartz, J. P. Eastwood, T. D. Phan, F. S. Mozer, J. Drake, M. A. Shay, P. A. Cassak, R. Nakamura, and G. Marklund (2016), Magnetospheric multiscale satellites observations of parallel electric fields associated with magnetic reconnection, *Phys. Rev. Lett.*, *116*, 235,102, doi:10.1103/PhysRevLett.116.235102.

[7] Ergun, R. E., L. J. Chen, F. D. Wilder, N. Ahmadi, S. Eriksson, M. E. Usanova, K. A. Goodrich, J. C. Holmes, A. P. Sturner, D. M. Malaspina, D. L. Newman, R. B. Torbert, M. Argall, P.-A. Lindqvist, J. L. Burch, J. M. Webster, J. F. Drake, L. M. Price, P. A. Cassak, M. Swisdak, M. A. Shay, D. B. Graham, R. J. Strangeway, C. T. Russell, B. L. Giles, J. C. Dorelli, D. Gershman, L. Avanov, M. Hesse, B. Lavraud, O. Le Contel, A. Retino, T. D. Phan, M. V. Goldman, J. E. Stawarz, S. J. Schwartz, J. P. Eastwood, K.-J. Hwang, R. Nakamura, and S. Wang (2017), Drift waves, intense parallel electric fields, and turbulence associated with asymmetric magnetic reconnection at the magnetopause, *Geophysical Research Letters*, doi:10.1002/2016GL072493, 2016GL072493.

[8] Huba, J. D., N. T. Gladd, and J. F. Drake (1982), The lower hybrid drift instability in nonantiparallel reversed field plasmas, *Journal of Geophysical Research: Space Physics*, *87*(A3), 1697–1701, doi:10.1029/JA087iA03p01697.

[9] Ji, H., S. Terry, M. Yamada, R. Kulsrud, A. Kuritsyn, and Y. Ren (2004), Electromagnetic fluctuations during fast reconnection in a laboratory plasma, *Phys. Rev. Lett.*, *92*(11), 115001, doi:10.1103/PhysRevLett.92.115001.

[10] Le, A., W. Daughton, L.-J. Chen, and J. Egedal (2017), Enhanced electron mixing and heating in 3-d asymmetric reconnection at the earth's magnetopause, *Geophysical Research Letters*, doi:10.1002/2017GL072522, 2017GL072522.

[11] Phan, T. D., G. Paschmann, C. Twitty, F. S. Mozer, J. T. Gosling, J. P. Eastwood, M. Øieroset, H. Rème, and E. A. Lucek (2007), Evidence of magnetic reconnection initiated in the magnetosheath, *Geophys. Res. Lett.*, L14104, doi:10.1029/2007GL030343.

[12] Price, L., M. Swisdak, J. F. Drake, P. A. Cassak, J. T. Dahlin, and R. E. Ergun (2016), The effects of turbulence on three-dimensional magnetic reconnection at the magnetopause, *Geophys. Res. Lett.*, *43*, doi:

10.1002/2016GL069578.

[13] Pritchett, P. L., F. S. Mozer, and M. Wilber (2012), Intense perpendicular electric fields associated with three-dimensional magnetic reconnection at the subsolar magnetopause, *J. Geophys. Res.*, *117*, A06212, doi: 10.1029/2012JA017533.

[14] Ren, Y., M. Yamada, H. Ji, S. P. Gerhardt, and R. Kulsrud (2008), Identification of the electron-diffusion region during magnetic reconnection in a laboratory plasma, *Phys. Rev. Lett.*, *101*, 085,003, doi: 10.1103/PhysRevLett.101.085003.

[15] Roytershteyn, V., W. Daughton, H. Karimabadi, and F. S. Mozer (2012), Influence of the lower-hybrid drift instability on magnetic reconnection in asymmetric configurations, *Phys. Rev. Lett.*, *108*, 185001, doi: 10.1103/PhysRevLett.108.185001.

[16] Winske, D. (1981), Current-driven microinstabilities in a neutral sheet, *The Physics of Fluids*, *24*(6), 1069–1076, doi:10.1063/1.863485.

[17] Wu, C. S., Y. M. Zhou, S. Tsai, S. C. Guo, D. Winske, and K. Papadopoulos (1983), A kinetic cross-field streaming instability, *The Physics of Fluids*, *26*(5), 1259–1267, doi:10.1063/1.864285.

[18] Yoon, P. H., Y. Lin, X. Y. Wang, and A. T. Y. Lui (2008), Theory and simulation of lower-hybrid drift instability for current sheet with guide field, *Physics of Plasmas*, *15*(11), 112,103, doi:10.1063/1.3013451.

[19] Zeiler, A., D. Biskamp, J. F. Drake, B. N. Rogers, M. A. Shay, and M. Scholer (2002), Three-dimensional particle simulations of collisionless magnetic reconnection, *J. Geophys. Res.*, *107*(A9), 1230, doi: 10.1029/2001JA000287.